



Full Length Article

Experimental evaluation of the performance of a novel planar segmented HPGe detector for use in gamma emission tomography

V. Rathore^{*}, L. Senis, A. Håkansson, E.A. Sundén, P. Andersson

Department of Physics and Astronomy, Uppsala University, Sweden

ARTICLE INFO

Keywords:

Segmented HPGe
Gamma spectroscopy
Gamma emission tomography
MCNP
Post-irradiation examination

ABSTRACT

The use of segmented HPGe detectors for gamma-ray tracking applications is well established. The spectroscopic capabilities of these detectors make them most suitable for such applications. For similar reasons, the use of such detectors in the tomographic measurement of irradiated nuclear fuel has also been envisioned. Especially, these detectors can facilitate faster fuel examination with excellent energy resolution. We have proposed and designed a novel planar segmented HPGe detector for use in gamma emission tomography. The design of the detector segmentation and the mode of operation is unique and offers six simultaneous detection channels for tomographic measurements. This work reports the first experimental evaluation of the performance of the detector. Important characteristics of the detector have been obtained, such as energy resolution of the segments in 1-fold (one segment) and 2-fold (two segments) modes, throughput curves, crosstalk energy corrections, and mislocalisation rate. Collimated source tests have been performed and the results have been compared with the MCNP simulations results. The obtained results are as expected and in good agreement with the simulation results, and it is estimated that using this detector can speed up the data collection by 3.2 times in comparison to an unsegmented detector of the same overall dimensions, in a tomographic application. Further improvements are foreseeable if scaling up to a larger detector with greater segmentation.

1. Introduction

Gamma emission tomography (GET), is a non-invasive technique for post-irradiation examination of nuclear fuel. The spatial distribution of gamma-emitting radionuclides is revealed in the reconstructed image from GET, which gives information on the fuel performance properties [1,2] such as burnup and power distributions, and on other phenomena relevant to fuel performance, such as fission product migration, fission gas release, and fuel fragmentation, relocation and dispersal [1,3–8]. The precision with which these fuel performance parameters can be quantified depends on the reconstructed image resolution, which in turn depends on various limitations and is subject to trade-offs with other requirements set by the investigation [9–11]. In addition, the energy resolution of the detector limits which peaks from a complex spectrum of irradiated nuclear fuel can be used for image reconstruction. On the other hand, the detection efficiency of the detector defines the minimum time required to complete the measurement with desired precision in the measured data. There is a conflict between requirements on high spatial resolution and maintaining a short measurement time [12,13], and therefore the use of a segmented HPGe detector combined with a multi-slit collimator has been proposed [13,14] to allow for simultaneous data collection at

multiple positions and thereby shorten the total measurement time, and also maintaining an excellent energy resolution.

Although segmented HPGe detectors are in use for many years in gamma-ray tracking and imaging applications [15,16], their use in the post-irradiation examination of nuclear fuel has not been explored. In this work, the experimental characterisation of the previously proposed [14] planar segmented HPGe detector is reported. The proposed detector is unique in its segmentation pattern and proposed mode of operation, and is aimed at demonstrating the use of segmented detectors to speed up data collection in gamma emission tomography of irradiated nuclear fuel, which can, in turn, be used to increase the obtainable spatial resolution. The detector presented in this study is a planar segmented HPGe detector, manufactured by Mirion Technologies. It is a scaled-down demonstration detector that has a comparatively lower cost and a less complex manufacturing process than the full-scale coaxial detector [13]. The demonstration detector has a planar design consisting of 7 segments, and the mode of operation is similar to what was proposed in [13] for a segmented coaxial detector.

A previous simulation study [14] describes the mode of operation and predicted performance parameters such as the efficiency and mislocalisation rate of the proposed detector. In this work, we present

^{*} Corresponding author.

E-mail address: vikram.rathore@physics.uu.se (V. Rathore).

experimental results to deduce important characteristics of the detector such as energy resolution, detection efficiencies, throughput curves, count rate limits, and mislocalisation rate. These tests are necessary to understand the behaviour and performance of such detectors [17,18] before their intended use in different applications.

Notably, the performance of segmented detectors can be affected by electronic crosstalk [19–23] which is unavoidable in such detectors. Unless addressed, this phenomenon can cause degradation of energy resolution and throughput performance. In this work, the experimental characterisation of the planar segmented HPGe detector is presented, and the performance is compared with predictions based on simulation results. A correction procedure for the crosstalk is described and evaluated.

2. Detector and data acquisition system

The detector is manufactured by Mirion Technologies as per the dimensions given in [14]. A schematic diagram of the detector active volume and its segmentation is shown in Fig. 1, and Fig. 2 shows a photo of the detector. The active volume has the dimensions $47 \times 44 \times 30 \text{ mm}^3$ with 2 mm passivation and a 3 mm guard ring surrounding the crystal on the non-contact sides resulting in overall crystal dimensions of $57 \times 54 \times 30 \text{ mm}^3$. The interelectrode gap width is approximately 0.35 mm. The bulk crystal is of p-type with an impurity concentration of $0.32 \times 10^{10}/\text{cm}^3$. The detector crystal is housed inside an aluminium enclosure with an entrance window thickness of 1 mm. The DC coupled front electrode (cathode, hole collecting electrode) is segmented into 7 segments. These are aligned with collimator slits in the proposed application and are intended to provide the location of incident gamma rays that interact in the detector. The back electrode (anode, electron collecting electrode) is AC coupled and provides information on the full active volume of the detector. The total energy for an event, which is needed for spectroscopic analysis, can either be obtained from the back electrode (full volume) or from the addback (sum) of the energies of the hit front segments. Each of the front segments and the back is coupled with a cold input stage charge-sensitive PSC823C preamplifier with a gain of 250 mV/MeV. The detector is positively biased with a voltage of 3000 V (applied at the back full volume electrode) and cooled by liquid nitrogen utilising a multi-attitude dewar.

The preamplifier output was read by CAEN V1782 8-channel 32k digital MCA (Multichannel Analyser). Each channel of the digitiser is equipped with a 16-bit 100 MS/s flash ADC (Analog to Digital Converter). The digitiser has onboard digital pulse processing capabilities which include a trapezoidal filter for energy determination, and a timing filter for timestamp generation. The acquisition and pulse processing parameters such as discriminator level, trapezoid rise time, etc., can be adjusted by the DAQ (Data Acquisition) software (CoMPASS v2.1 provided by CAEN) GUI interface. In the list mode, timestamp, energy and/or waveform can be saved on an event-by-event basis. The software also provides an energy spectrum from each segment and the full volume back electrode.

3. Method

In the detector characterisation work, experiments were performed with and without the use of a collimator. Available standard laboratory sources ^{137}Cs , ^{60}Co , ^{207}Bi with activity in the kBq range were used. In all the experiments, data from the digitiser was saved in list mode with the help of DAQ software.

In a tomographic measurement, the detector will be used with a multi-slit (in total 6 slits) collimator [14]. The collimator slits will be centred on the respective detector segments (1 to 6), and the cross-sectional area of the slits will be such that only a small area in the centre of the small segments will be directly irradiated and segment-7 will remain outside the direct irradiation paths, only subjected to scattered photons and secondary radiation. To assign the location of an

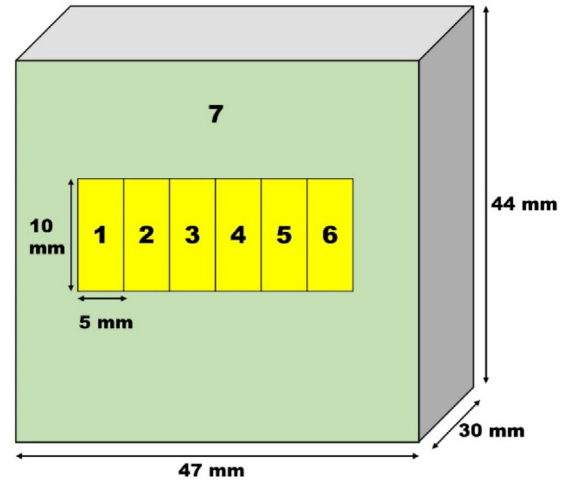


Fig. 1. Schematic diagram of the planar segmented HPGe detector crystal. The front electrode is segmented into seven segments, 6 small segments of equal dimensions for the assignment of incident photons with respective collimator slits of entry, and the outer big segment facilitates full energy deposition of photons scattered in and escaping from the small segments.

incoming photon to a slit/segment and determine the total deposited energy, different methods can be used as described in [13]. In this work, we have used the following method (Table 1) to assign an event to a segment and determine the corresponding energy based on different scenarios. Although this method discards a fraction of events that deposit their full energy in the full volume of the detector, the mislocalisation rate was found to be the least using this method [13]. Mislocalisation is an undesired event in which a photon deposits full energy in the detector but is assigned to a wrong slit position/segment. Such events can occur due to reasons such as coherent scattering, and transmission through the bulk of collimator material.

The performance in terms of energy resolution, and relative efficiency were obtained for different scenarios. The following terminology is used to refer to different energy spectra obtained based on the different scenarios.

- Single spectrum :** The energy spectrum of 1-fold events in the respective segments.
- Addback spectrum :** The energy spectrum of 2-fold events ($E_i + E_j$), where $i = 1$ to 6.
- Total spectrum :** The spectrum including both single and addback events, according to the above.

Please note that the fold here refers to the segment fold, within a segment a photon can have multiple interactions. To obtain 1-fold and 2-fold events and the corresponding energies, the list mode data from the digitiser was used to make a coincidence events matrix among all the segments (1 to 7, and the full volume) and events (1-fold and 2-fold) were selected for each small segment by applying the logical operations on the matrix.

Experiments without the use of a collimator were performed for a longer duration and the energy calibration for each segment was performed using 1-fold events in the respective segments. The energy resolution of each segment was obtained after performing the energy calibration. An addback spectrum for each small segment was obtained from the experimental data without using a collimator to observe the crosstalk effects and addback energy resolution obtainable before and after applying the correction. Crosstalk correction factors were also evaluated for each addback spectrum. To correct the energy spectrum for crosstalk, a method was obtained from [20]. The correction is based on calibrating a relationship between true and measured energy values, defined in a matrix form (Eq. (1)). The matrix element $E_{i \leftarrow j}$ denotes

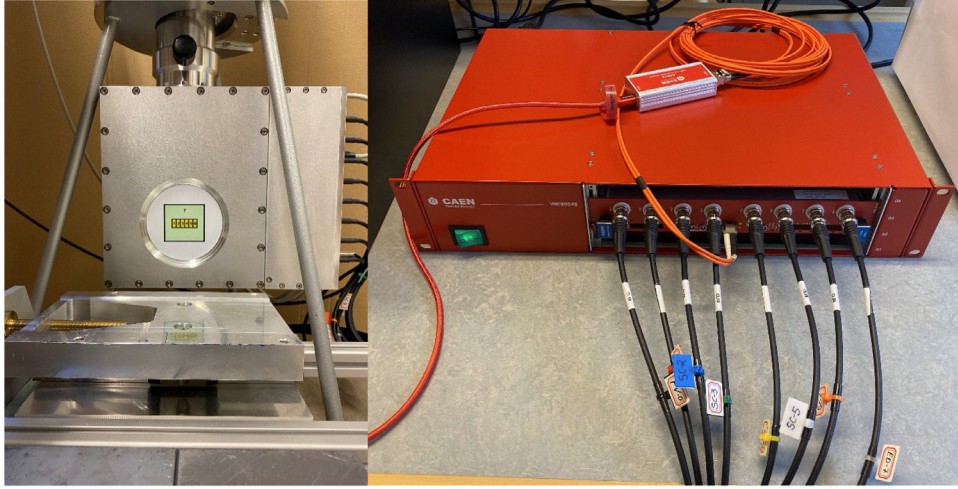


Fig. 2. Left — The planar segmented HPGe detector with ball screw sliding table placed in front for movement of collimated sources. A sticker depicting the segmentation pattern was put on the entrance window for segment identification and alignment purposes. Right — CAEN V1782 8-channel data acquisition system.

Table 1

Event localisation and energy determination based on different scenarios during a tomographic measurement. (Fired refers to a trigger threshold being passed).

Scenario	Event localisation and energy
Any one of the small segments (1 to 6) has fired	Fired segment and energy from the corresponding list data
Any one of the small segments (1 to 6) and segment-7 have fired in coincidence	Fired small segment and the sum of respective energies ($E_i + E_7$) from list data, i = index of the fired small segment
Two or more small segments have fired in coincidence	The event is discarded to avoid possible mislocalisation

the crosstalk coefficient for segment i for a gamma ray interaction in segment-7 and vice versa. These elements were determined from the intercepts of 661.7 keV diagonal line on the axes in a plot of 2-fold events between respective segments as shown in Fig. 3 (left). To obtain the intercepts on the axes the diagonal corresponding to 661.7 keV was extrapolated (by least square linear fit), Fig. 3 (right) shows the extrapolated diagonal line and the zoomed-in view of the intercepts on the axes. The correction matrix C was determined for each small segment (1 to 6) and segment-7 pair and inverted to obtain the true energy values. It should be noted here that unlike in [20] full volume-to-segment crosstalk effects were not considered.

$$\begin{pmatrix} E_i \\ E_7 \end{pmatrix}_{\text{meas}} = C \cdot \begin{pmatrix} E_i \\ E_7 \end{pmatrix}_{\text{true}}, i = 1 \text{ to } 6 \quad (1)$$

$$\text{where } C = \begin{pmatrix} 1 & E_{i \leftarrow 7} \\ E_{7 \leftarrow i} & 1 \end{pmatrix}.$$

To study the performance of the detector for the planned tomographic measurement of nuclear fuel, experiments were performed with a well-collimated source. A cylindrical tungsten collimator (50 mm diameter, 175 mm length) with a single circular slit (2 mm) was used. A ^{137}Cs source enclosed inside a lead cylinder with a circular opening was placed behind the collimator. The source and the collimator were mounted on a ball-screw linear sliding table which provided the translation motion in one dimension by rotating the screw of 1 mm pitch. The collimated source was centred on segment 1 and list data was acquired for 10 h, after finishing the acquisition the collimated source was moved to the centre of the next segment and the process was repeated. Six different datasets were thus obtained for six different collimated source positions. The data were analysed as described above to make singles, addback, and total (addback +singles) spectra.

Using a well-collimated source also presented an opportunity to test the mislocalisation. Since during each acquisition only a single segment

was irradiated directly by the source, any full energy events obtained in the total spectra of the remaining small segments were attributed to the mislocalisation. Since it was difficult to carry out the absolute and intrinsic efficiency calibration, relative comparisons (Table 4) between the experimental and simulation results were performed to assert the detector performance. Simulations were performed using particle transport code MCNP6.2 [24]. The detector crystal was modelled with an aluminium enclosure, and each small segment was irradiated with a photon beam of around 3.3 mm divergence at the back surface. Coincidence/anticoincidence logic was implemented in the simulated spectra using the MCNP FT PHL [25] option.

To evaluate the count rate capability of the detector, a two-source test was performed. The ^{137}Cs source was fixed in a position such that it caused an input count rate (ICR) near 2000 cps (counts per second), while the strong ^{60}Co source was moved to vary the total ICR up to $\sim 10^6$ cps in the full volume of the detector. The Full Width at Half Maximum (FWHM), the output count rate (OCR), and the peak energy of the ^{137}Cs were obtained (from the singles spectra) for each segment as well as the full volume. In all of the data analyses, a 10 keV energy threshold (for identification of singles as well as addback events in offline mode) was used to filter noise and false multifold events. For all the segments and the back electrode, a 6 μs rise time and 1 μs of flat top time were used for the trapezoidal filter. An RC-CR2 filter was used for the trigger and timing (timestamp generation) and the highest possible value of 32 samples was used as the fast discriminator smoothing factor [26] for all the segments and back electrode signals.

4. Results

4.1. Energy resolution and crosstalk corrections

The energy resolution of each segment and the full volume (back electrode) at energies 661.7, and 1332.5 keV was obtained after

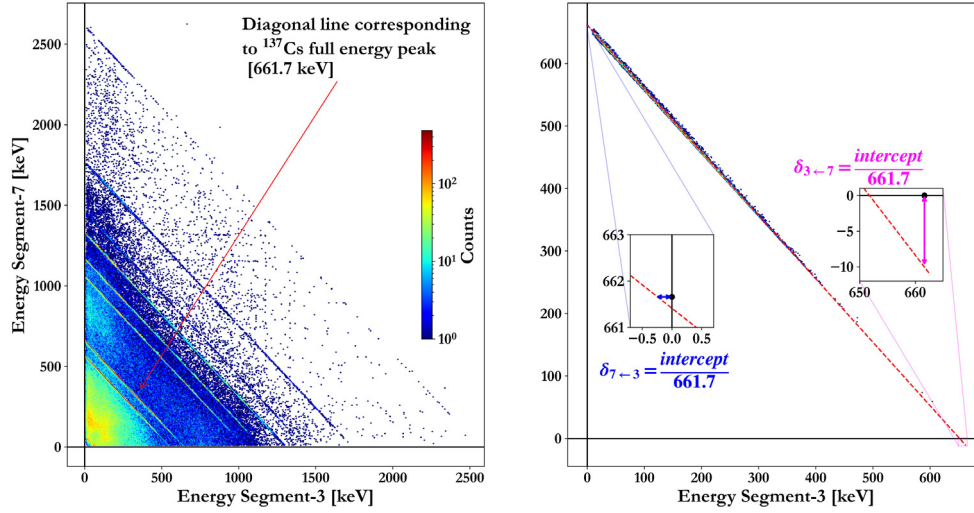


Fig. 3. Left – A plot of 2-fold events between segment-3 and segment-7, diagonal lines represent energy correlation due to Compton scattering in the respective segments for energy lines from ^{207}Bi , ^{137}Cs , and ^{60}Co . Due to electronic crosstalk, the diagonal lines deviate from the location of full energy peaks in the singles spectra, a diagonal line for 661.7 keV was extrapolated and the deviation is visible in the zoomed-in plot on the right. Right — Zoomed-in 661.7 keV line with intercepts on the respective axes for determination of correction matrix elements δ_{3-7} and δ_{7-3} .

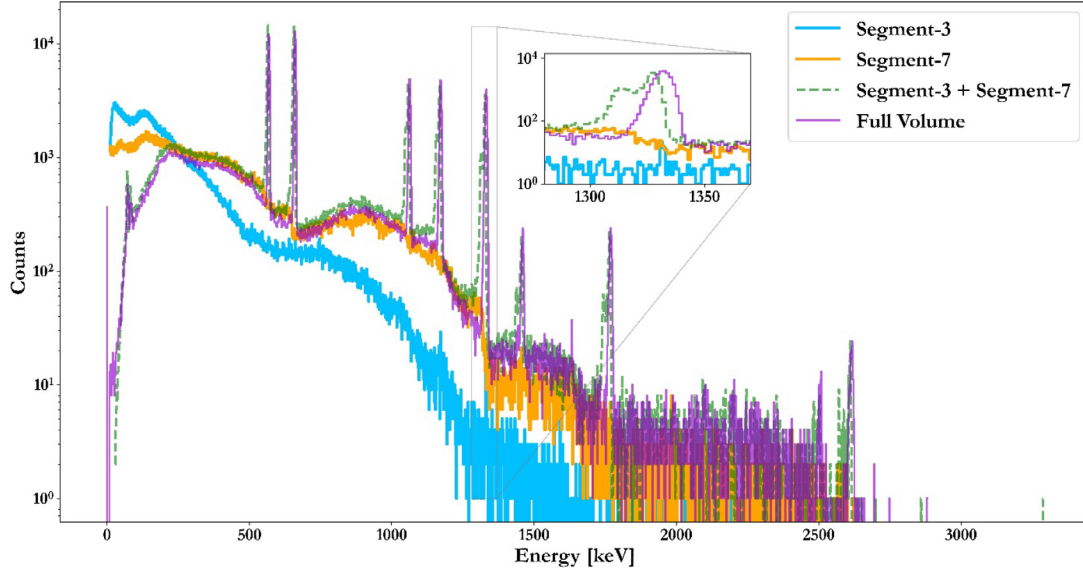


Fig. 4. Energy spectra of the measured 2-fold events in segment pair (3, 7) without crosstalk correction. The peaks in the addback (segment-3 + segment-7) spectrum are broadened, shifted and split in comparison to the peaks in the energy spectrum obtained from the full volume back electrode as seen in the zoomed-in view in the inset.

Table 2

Energy resolution (full width half maximum in keV) of every single segment and the back electrode obtained (1-fold events).

Energy [keV]	Full volume (FWHM)	Seg.-1 (FWHM)	Seg.-2 (FWHM)	Seg.-3 (FWHM)	Seg.-4 (FWHM)	Seg.-5 (FWHM)	Seg.-6 (FWHM)	Seg.-7 (FWHM)
@662	5.55	1.33	1.30	1.34	1.32	1.32	1.33	2.10
@1332	7.57	1.74	1.72	1.73	1.73	1.73	1.73	2.55

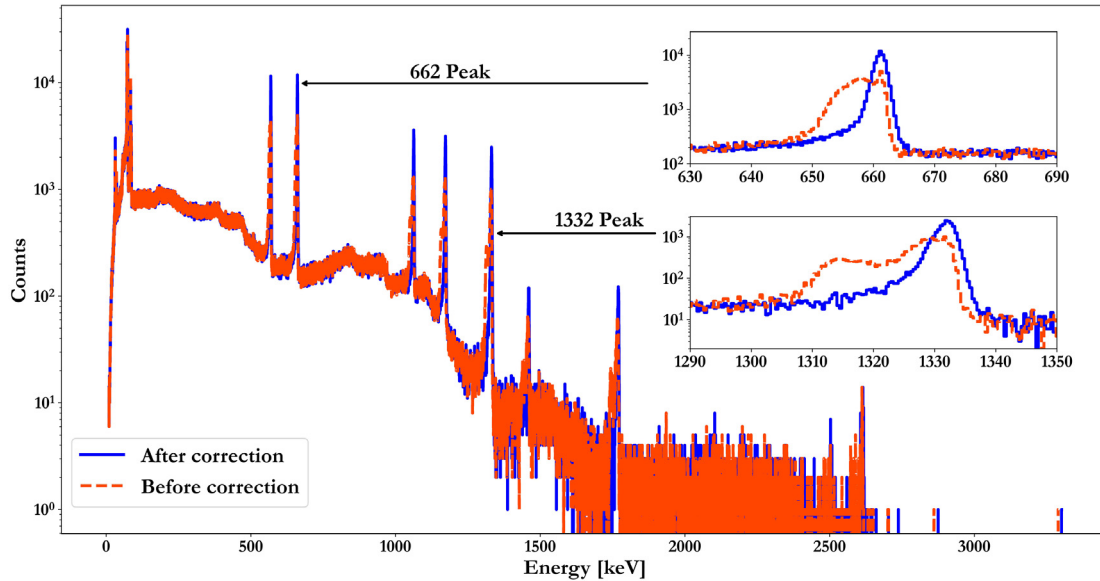
performing the energy calibration using 1-fold events and shown in Table 2. The energy resolution of segments 1 to 7 is reasonably good and comparable to what might be expected in a conventional HPGe detector. The energy resolution of the full volume is degraded. Some plausible explanations for the worse energy resolution of the back electrode are the high capacitance of the full volume in comparison to the segments, and the crosstalk from the segments to the back electrode. However, for better full volume resolution, the energy information of an event can also be obtained from the addback spectra of segments 1 to 7 as mentioned in Section 2, and this strategy was chosen since it provided better energy resolution.

Energy spectra of the measured 2-fold events for segment pair (3, 7) were plotted and shown in Fig. 4, it shows the spectrum of energies in segment-3, segment-7, the respective sum (or addback), and the corresponding energies obtained from the full volume back electrode. Due to electronic crosstalk which is proportional [27–29] in nature, the energy values obtained in the segments were different from the actual energy deposition during the gamma-ray interactions in the respective segments. This results in peak broadening, non-Gaussian peak shape, and an energy shift in the addback spectrum as seen in Fig. 4. Similar effects were observed in the measured addback spectra of the other segment pairs. In terms of percentage of the deposited energy, the

Table 3

Energy resolution in total spectra of the segment pairs before and after applying the crosstalk corrections.

Segment pair	FWHM [keV] @662 keV		FWHM [keV] @1332 keV	
	Before correction	After correction	Before correction	After correction
(1, 7)	6.78	2.21	6.13	3.30
(2, 7)	7.46	2.06	7.00	3.22
(3, 7)	7.38	2.08	6.95	3.20
(4, 7)	7.10	2.04	6.84	3.05
(5, 7)	6.99	2.02	6.64	2.91
(6, 7)	6.38	2.07	5.99	2.99

**Fig. 5.** Total spectra of segment pair (3, 7) before and after applying the crosstalk correction, zoomed-in peaks in the insets.

crosstalk shifts were obtained at about 1.57% for the segment pairs (1, 7) and (6, 7) and about 1.5% for the segment pairs (2, 7), (3, 7), (4, 7), and (5, 7). A peak-to-peak noise assessment was also made for all the segments and the full volume contact, the average peak-to-peak noise in segments 1 to 6 was obtained ~ 6 keV, for segment-7 ~ 9 keV, and full volume contact ~ 13 keV.

The total spectrum for segment pair (3, 7) was plotted before and after applying the correction as shown in Fig. 5. The energy resolution of the total spectra after implementing the crosstalk corrections (Table 3) was obtained in the range 2.0–2.2 keV at 662 keV, and 3.0–3.3 keV at 1332 keV for segment pairs (1, 7) to (6, 7). The energy resolution of the total spectra is not as good as the energy resolution of 1-fold events given in Table 2, but still representative of an HPGe detector.

4.2. Count rate capabilities

Fig. 6 shows the throughput curve for all the segments and the full volume, ICR for the full volume has reached up to 1.8×10^5 cps and up to 1.3×10^5 cps for segment-7. The full volume and segment-7 maintained a linear OCR for ICR of up to 20 000 cps, in the small segments the maximum ICR reached approximately 4000 cps and the OCR remained linear for that range. Although the dead time of segment-7 and full volume has increased sharply after an ICR value of 20 000 cps, segment-7 will be well shielded during a tomographic measurement and the ICR is expected to remain below 20 000 cps. Fig. 7 shows the variation in FWHM at 662 keV with ICR for all the segments and the full volume. The resolution worsens as the ICR increases and is unacceptably large beyond 20 000 cps.

4.3. Collimated source test and validation of simulation results

The data collected from six different collimated source positions were analysed to make 1-fold, 2-fold and total spectra for each small

Table 4

Compared quantities between the experimental and the simulation results.

Figure no.	Compared quantity for each segment under 662 keV peak
Fig. 8	Total counts/Max (Total counts)
Fig. 9	Singles counts/Total counts (Singles and addback)
Fig. 10	Total counts (Singles and addback)/Full volume counts
Fig. 11	Singles counts/Full volume counts
Fig. 12	Full volume counts/Max (Full Volume counts)

segment. Net counts in full energy peak of ^{137}Cs (661.7 keV) were obtained using the method of *peak area determination using extended background regions* as described in [30]. Similarly, counts from the simulated spectra were also obtained from the output files generated after each MCNP simulation. Fig. 8 shows the comparison of relative counts in full energy peak between MCNP and the experimental total spectra. To obtain the relative counts, counts in each small segment were divided by the maximum among them. The experimental results are in good agreement with MCNP results, and the behaviour is as expected between the segments. Segments 1 and 6 have higher counts (10%–11%) in comparison to segments 2–5, which is expected since more events are discarded in these segments. Events were discarded if two or more small segments have fired in coincidence, and for segments 2–5 this is more likely to happen as they share a major portion of their boundary with each other than 1 and 6.

The ratio of singles (1-fold) to total (1-fold and 2-fold) counts under the peak for each segment was obtained from the simulations and the experimental results and plotted (Fig. 9) for comparison. The behaviour is similar in both cases and the results are in good agreement between the experiment and simulation. The counts under the peak for full detector volume were obtained from the full volume spectra obtained in six different collimated source positions, each centred at

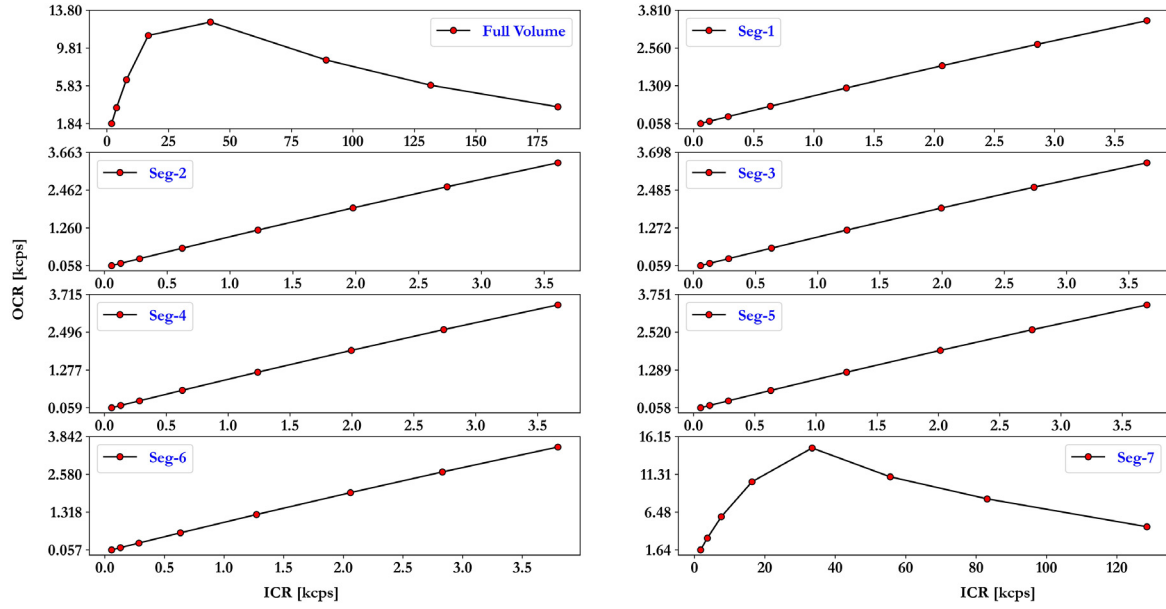


Fig. 6. Throughput curves for each segment and the full volume. Due to the small size of segments 1–6, it is difficult to impose a count rate that is near saturation.

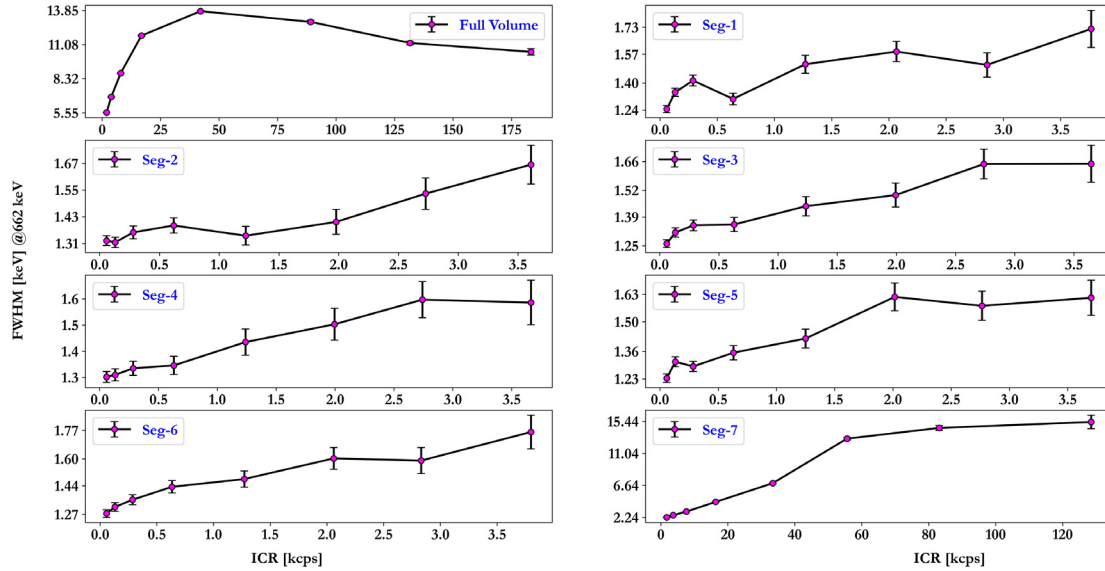


Fig. 7. The variation of FWHM @662 keV with input count rate (ICR).

one of the small segments. The ratios of total to full detector volume peak counts were calculated for all the small segments. Fig. 10 shows the comparison plot between MCNP and the experiment, the overall behaviour is again the same in both but the ratios are lower in the experimental results. For segments 1 and 6, it is less by 10%–12%, and by 7%–8% for segments 2 to 5.

Similarly, the ratio of peak counts from 1-fold spectrum to full detector volume spectrum for each segment was plotted, as shown in Fig. 11, for comparison between MCNP and experimental results. Also, in this case, the ratios are lower in the experimental results by 4%–5%. However, for comparison, the relative counts in the peak (counts/maximum) obtained from the full detector volume spectra were plotted (Fig. 12) and are in good agreement with the MCNP results. As expected the counts are slightly higher when the collimated source was centred on segments 2–5 this is because of a slightly higher

probability of interaction if a photon incident more towards the centre of the detector.

The mislocalisation rate per full energy event was determined for each source position from the total (1-fold +2-fold) spectra. In each source position, we obtained six different total spectra, one for each small segment. However, the counts observed under the peak in five (segments other than irradiated by the collimated source) out of six spectra correspond to the mislocalisation rate. Therefore, the sum of peak counts in the five segments divided by the sum of peak counts in all six segments was defined as the mislocalisation rate per full energy event. From the experimental results, this was obtained as 5–6 counts per 1000 full energy peak counts. Of these, ^{137}Cs in the lab background is responsible for 2–3 counts. The impact of this level of mislocalisation is considered acceptable for use in tomography.

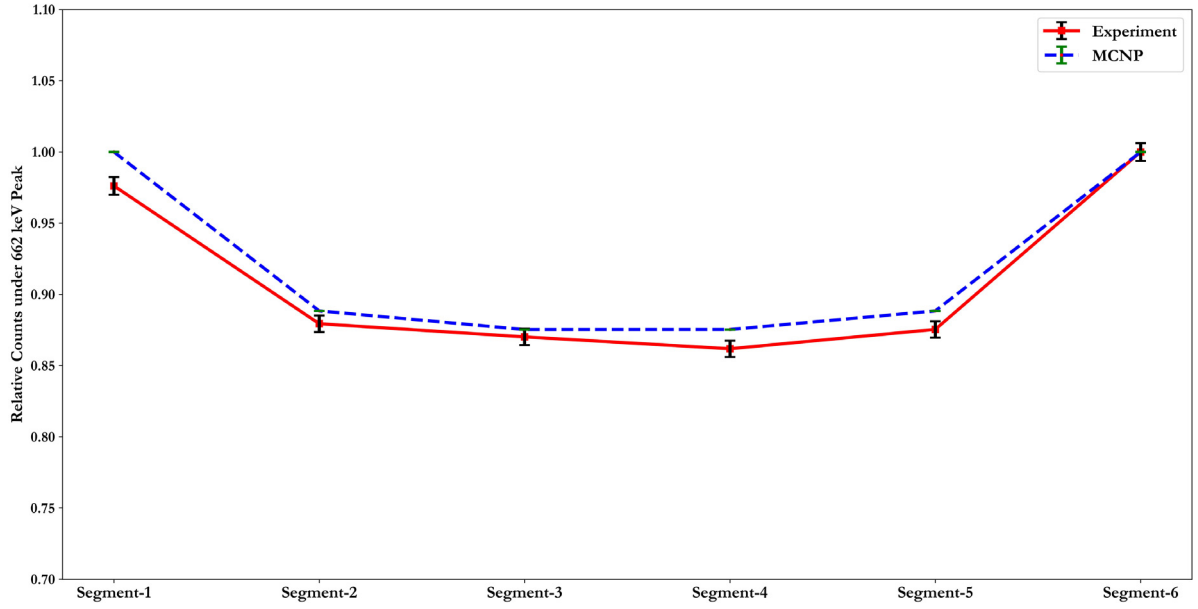


Fig. 8. Comparison of relative counts under 662 keV peak in the total spectrum (1-fold +2-fold) obtained for each segment from the experimental and MCNP results.

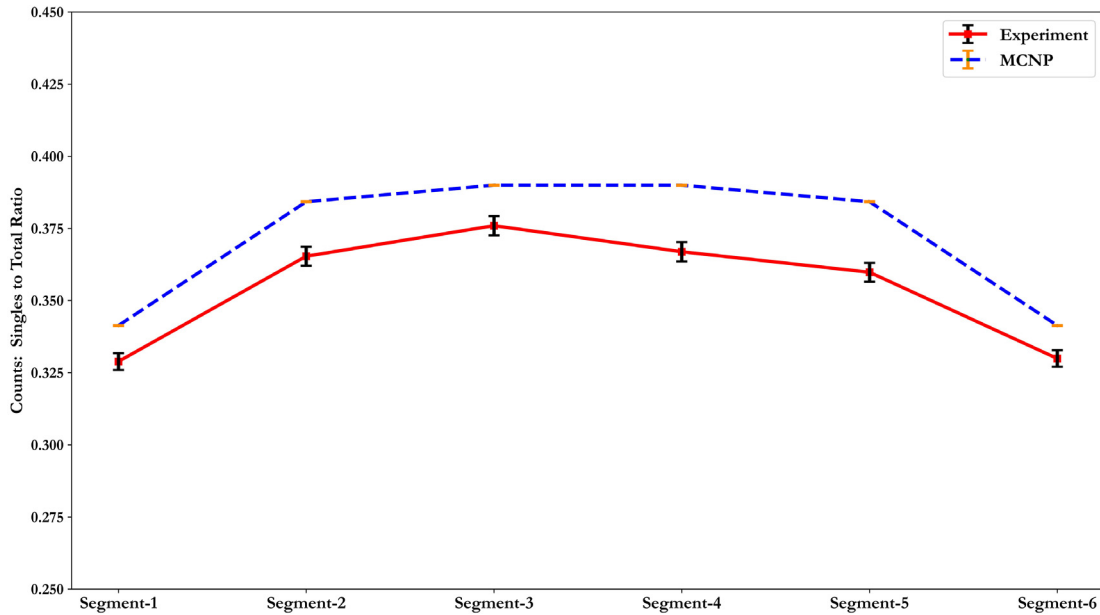


Fig. 9. Comparison of 1-fold to total (1-fold +2-fold) counts (under 662 keV peak) ratio obtained for each segment from the experimental and MCNP results.

5. Conclusions and outlook

Experimental evaluation of the properties of a novel planar segmented HPGe detector has been done in this work. The detector performance is found to be as expected and satisfactory with regard to its intended use in a tomographic measurement. The energy resolutions of the segments in individual detection mode (1-folds in the respective segments) were found to be excellent, while also reasonably good in the addback mode with the large segment after making corrections for the crosstalk effects. The performance of the detector in terms of count rate limits and energy resolution did not degrade much up to a total ICR of 20 000 cps in the full volume. This covers the anticipated typical count rate of the proposed tomographic application.

The detector performance shows a good agreement with the MCNP predictions. Considering the lowest total (1-fold +2-fold) counts to full

detector volume counts ratio of 53% for the middle segments, this detector will be overall 3.2 (53% times 6 segments) times faster than a detector of the same overall dimensions without segmentation, which would require multiple steps to obtain the information equivalent to a single examination with the segmented detector. Using this detector, roughly a 24 h measurement can be completed in less than 8 h or less if the number of segments is increased. This might be significant and can facilitate achieving a higher spatial resolution in GET, by allowing time for more positions to be acquired. The mislocalisation rate was found nearly negligible which affirmed the ability of the segments to work as individual detection elements, as if using a conventional unsegmented detector moved in six times as many steps.

The energy resolution of the full volume signal was rather dissatisfactory. This should however not be a concern as the energy

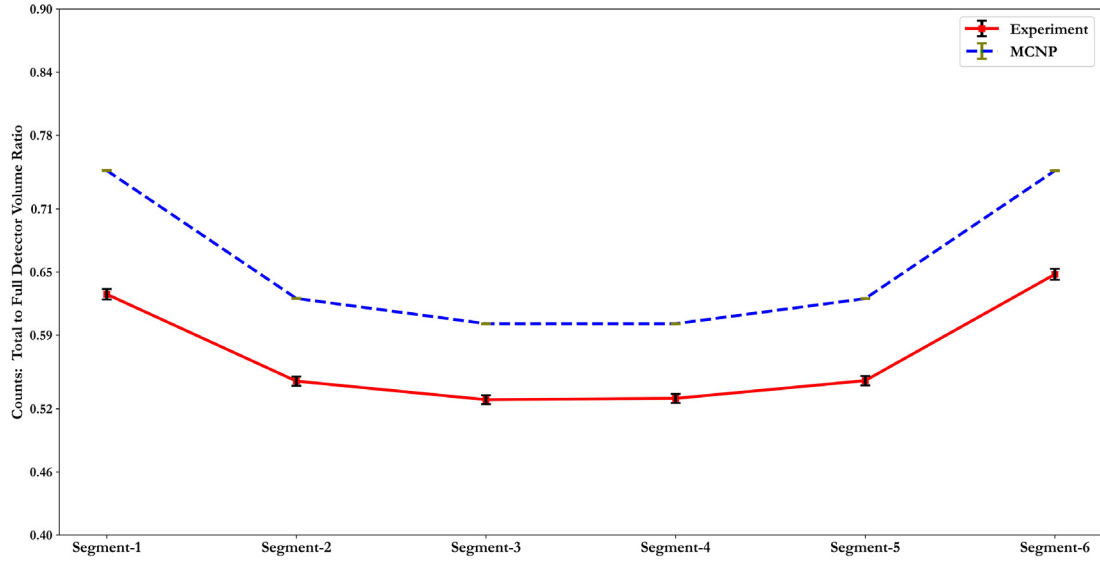


Fig. 10. Comparison of the ratio of total (1-fold +2-fold) to full detector volume counts under 662 keV peak obtained for each segment from the experimental and MCNP results.

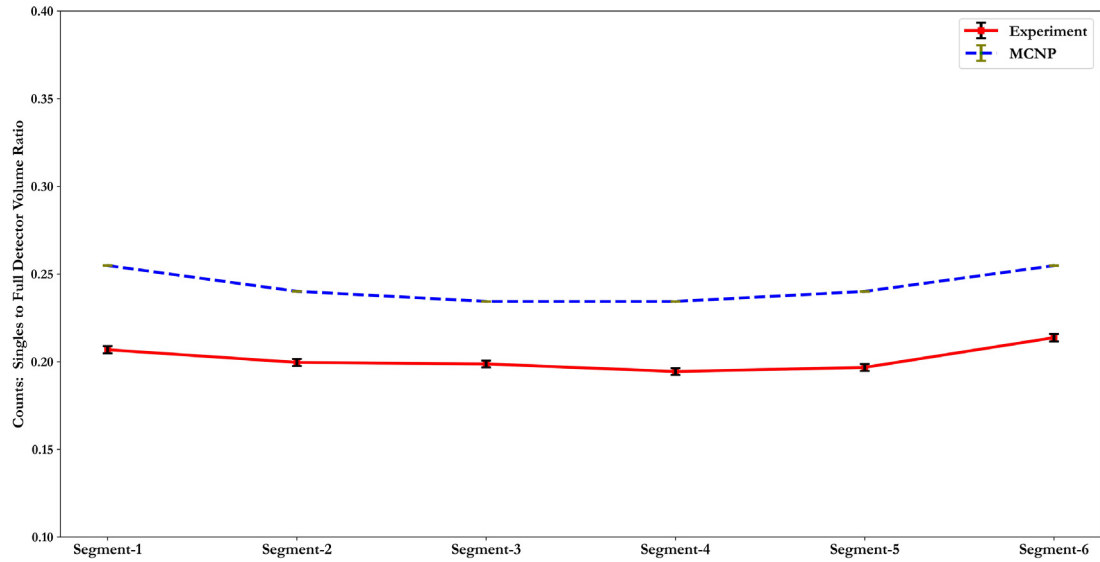


Fig. 11. Comparison of the ratio of 1-fold to full detector volume peak counts obtained for each segment from the experimental and MCNP results.

information can be obtained from the addback of the segmented electrodes, however, the full volume resolution may be possible to improve by careful investigation of the underlying causes and remediation using appropriate corrections. The acquisition and the digital pulse processing parameters such as setting the right energy threshold, trapezoidal rise time, baseline smoothing, etc., were not carefully optimised, and the performance (energy resolution, dead time, etc.) can be improved by doing so. In particular, it should be noted that the fast discriminator smoothing factor [26] for the trigger threshold was found to be important to avoid erroneous rejection of 2-fold events that may otherwise be flagged as pileup, due to transient cross talk. The addback mode in this work was considered only between the bigger (segment-7) and small segments (1 to 6) pair which is the mode of operation with the lowest mislocalisation rate. The addback between all possible segment pairs can also be obtained to recover all the full energy peak counts in the detector, however, for that purpose, a full crosstalk correction matrix (of size 7×7) needs to be determined. An all-segment

addback would improve the overall detection efficiency, but the mislocalisation rate also increases as shown in [13], and it would thus be detrimental to the ability to correctly localise the segment of the first entrance.

The detector performance for tomographic measurement agreed well with the MCNP results, the underestimation of the 1-fold and total counts in the respective segments in the experimental results could be due to reasons such as improper alignment of the collimated source and the segment centre, erroneous pileup rejection of events for the DC coupled front segments, low energy scatter events in coincidence with subsequent absorption in the segment-7 were not recorded during the online data acquisition in the small segments. It is therefore important that a proper alignment should be achieved before starting the actual tomographic measurement, and optimum acquisition settings should be applied according to the measurement conditions.

Following these promising results, tests in a GET setup will be performed with the BETTAN (the name of a laboratory device at

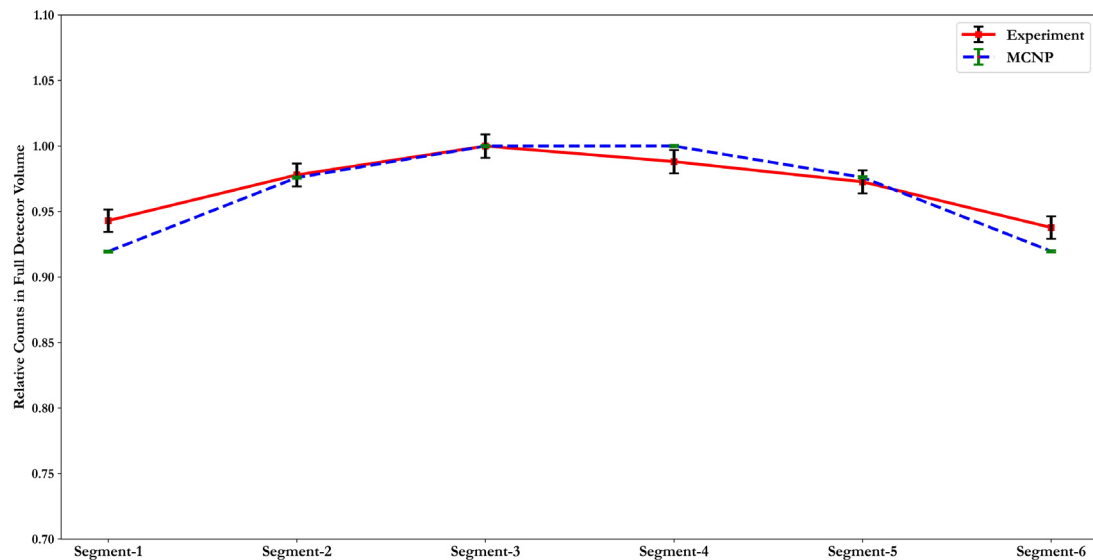


Fig. 12. Comparison of relative peak counts in full detector volume spectrum obtained for each collimated source position (centred on a small segment) from the experimental and MCNP results.

the department of physics for tomography measurements [31]) tomography workbench at Uppsala University. The preparations for the final demonstration of the detector for tomographic measurements are undergoing.

Declaration of competing interest

The authors declare that they have no known competing financial interests or personal relationships that could have appeared to influence the work reported in this paper.

Data availability

Data will be made available on request.

Acknowledgements

This work is financially supported by the Swedish Research Council, grant number 2017-06448, and by the Swedish Foundation for Strategic Research, grant number EM-16-0031. We would also like to express our gratitude to Studsvik AB, Sweden, for lending the collimator used in the experiments.

References

- [1] S. Holcombe, S. Jacobsson Svärd, L. Hallstadius, A Novel gamma emission tomography instrument for enhanced fuel characterization capabilities within the OECD Halden Reactor Project, *Ann. Nucl. Energy* 85 (2015) 837–845, <http://dx.doi.org/10.1016/j.anucene.2015.06.043>.
- [2] S. Kilby, et al., Multi-modal tomographic imaging system for poolside characterization of nuclear test fuels: Design considerations and studies, *Nucl. Instrum. Methods Phys. Res. A* 1045 (2023) 167553, <http://dx.doi.org/10.1016/j.nima.2022.167553>.
- [3] S. Caruso, M.F. Murphy, F. Jatuff, R. Chawla, Nondestructive determination of fresh and spent nuclear fuel rod density distributions through computerised gamma-ray transmission tomography, *J. Nucl. Sci. Technol.* 45 (8) (2008) 828–835, <http://dx.doi.org/10.1080/18811248.2008.9711484>.
- [4] S.T. Hsue, T.W. Crane, J. Talbert, J.C. Lee, Nondestructive Assay Methods for Irradiated Nuclear Fuels, Los Alamos Scientific Lab., N.Mex. (USA), LA-6923, 1978, <http://dx.doi.org/10.2172/5153553>.
- [5] P. Jansson, S.J. Svärd, A. Håkansson, A. Bäcklin, A device for nondestructive experimental determination of the power distribution in a nuclear fuel assembly, *Nucl. Sci. Eng.* 152 (1) (2006) 76–86, <http://dx.doi.org/10.13182/NSE06-A2565>.
- [6] P. Andersson, S. Holcombe, T. Tverberg, Inspection of a LOCA test rod at the Halden reactor project using gamma emission tomography, 2016, [Online]. Available: <http://urn.kb.se/resolve?urn=urn:nbn:se:uu:diva-303810>.
- [7] B. Biard, Quantitative analysis of the fission product distribution in a damaged fuel assembly using gamma-spectrometry and computed tomography for the Phébus FPT3 test, *Nucl. Eng. Des.* 262 (2013) 469–483, <http://dx.doi.org/10.1016/j.nucengdes.2013.05.019>.
- [8] J. Schulthess, et al., Non-destructive post-irradiation examination results of the first modern fueled experiments in TREAT, *J. Nucl. Mater.* 541 (2020) 152442, <http://dx.doi.org/10.1016/j.jnucmat.2020.152442>.
- [9] L. Senis, et al., Evaluation of gamma-ray transmission through rectangular collimator slits for application in nuclear fuel spectrometry, *Nucl. Instrum. Methods Phys. Res. A* (2021) 165698, <http://dx.doi.org/10.1016/j.nima.2021.165698>.
- [10] L. Senis, et al., Feasibility study of gamma-ray micro-densitometry for the examination of nuclear fuel swelling, in: Presented at the Top Fuel 2021, Santander, Spain, 24–28 October 2021, 2021, [Online]. Available: <http://urn.kb.se/resolve?urn=urn:nbn:se:uu:diva-442645>.
- [11] L. Senis, et al., A computational methodology for estimating the detected energy spectra of the gamma-ray flux from irradiated nuclear fuel, *IEEE Trans. Nucl. Sci.* 69 (4) (2022) 703–713, <http://dx.doi.org/10.1109/TNS.2022.3152264>.
- [12] Industrial process gamma tomography, Vienna, IAEA–TECDOC-1589, 2008, [Online]. Available: https://www-pub.iaea.org/MTCD/Publications/PDF/TE_1589_web.pdf.
- [13] P. Andersson, et al., Simulation of the response of a segmented high-purity germanium detector for gamma emission tomography of nuclear fuel, *SN Appl. Sci.* 2 (2) (2020) 271, <http://dx.doi.org/10.1007/s42452-020-2053-4>.
- [14] V. Rathore, L. Senis, P. Jansson, E.A. Sundén, A. Håkansson, P. Andersson, Calculation of spatial response of a collimated segmented HPGe detector for gamma emission tomography by MCNP simulations, *IEEE Trans. Nucl. Sci.* (2022) 1, <http://dx.doi.org/10.1109/TNS.2022.3152056>.
- [15] S. Akkoyun, et al., AGATA—Advanced gamma tracking array, *Nucl. Instrum. Methods Phys. Res. A* 668 (2012) 26–58, <http://dx.doi.org/10.1016/j.nima.2011.11.081>.
- [16] S. Paschalis, et al., The performance of the gamma-ray energy tracking in-beam nuclear array GRETINA, *Nucl. Instrum. Methods Phys. Res. A* 709 (2013) 44–55, <http://dx.doi.org/10.1016/j.nima.2013.01.009>.
- [17] E. Rintoul, et al., Simulation and validation of a planar HPGe detector signal database for use in pulse shape analysis, *Nucl. Instrum. Methods Phys. Res. A* 1034 (2022) 166641, <http://dx.doi.org/10.1016/j.nima.2022.166641>.
- [18] F.J. Pearce, et al., First experimental measurements with the Segmented Inverted-coaxial GerMANium (SIGMA) detector, *Nucl. Instrum. Methods Phys. Res. A* 1027 (2022) 166044, <http://dx.doi.org/10.1016/j.nima.2021.166044>.
- [19] B. Bruyneel, et al., Crosstalk properties of 36-fold segmented symmetric hexagonal HPGe detectors, *Nucl. Instrum. Methods Phys. Res. A* 599 (2) (2009) 196–208, <http://dx.doi.org/10.1016/j.nima.2008.11.011>.
- [20] B. Bruyneel, et al., Crosstalk corrections for improved energy resolution with highly segmented HPGe-detectors, *Nucl. Instrum. Methods Phys. Res. A* 608 (1) (2009) 99–106, <http://dx.doi.org/10.1016/j.nima.2009.06.037>.
- [21] A. Pullia, D. Weisshaar, F. Zocca, D. Bazzacco, Cross-talk limits of highly segmented semiconductor detectors, *IEEE Trans. Nucl. Sci.* 58 (3) (2011) 1201–1205, <http://dx.doi.org/10.1109/TNS.2011.2129530>.

- [22] B. Bruyneel, P. Reiter, G. Pascovici, Characterization of large volume HPGe detectors. Part I: Electron and hole mobility parameterization, Nucl. Instrum. Methods Phys. Res. A 569 (3) (2006) 764–773, <http://dx.doi.org/10.1016/j.nima.2006.08.130>.
- [23] J. Han, K.B. Lee, J.-M. Lee, S.H. Lee, T.S. Park, J.S. Oh, Locating events in a segment of a segmented HPGe detector at KRISS, Nucl. Instrum. Methods Phys. Res. A 948 (2019) 162680, <http://dx.doi.org/10.1016/j.nima.2019.162680>.
- [24] C.J. Werner (Ed.), MCNP6.2 Release Notes, Report LA-UR-18-20808, Los Alamos National Laboratory, 2018.
- [25] C.J. Werner (Ed.), MCNP Users Manual - Code Version 6.2, Report LA-UR-17-29981, Los Alamos National Laboratory, 2017.
- [26] CoMPASS Quick Start Guide, GD6300, CAEN S.p.A., 2022.
- [27] T.D. Bucher, et al., Proportional crosstalk correction for the segmented clover at iThemba LABS, Phys. Scr. 92 (11) (2017) 114004, <http://dx.doi.org/10.1088/1402-4896/aa8e29>.
- [28] A. Caffrey, The Development and Evaluation of a Compton Camera for Imaging Spent Fuel Rod Assemblies (Ph.D. thesis), University of Liverpool, 2019, [Online]. Available: <https://livrepository.liverpool.ac.uk/3070060>.
- [29] E.J. Rintoul, Characterisation of an Electrically Cooled Planar Germanium Detector for Use in the GRI+ Compton Camera System, University of Liverpool, 2020, [Online]. Available: https://livrepository.liverpool.ac.uk/3106394/1/200777228_2020.pdf.
- [30] G. Gilmore, Chapter 5 : Statistics of Counting, in Practical Gamma-Ray Spectrometry, second ed., Wiley, West Sussex, 2011, pp. 101–126.
- [31] P. Jansson, S. Grape, S. Jacobsson Svård, A. Håkansson, A laboratory device for developing analysis tools and methods for gamma emission tomography of nuclear fuel, presented at the the 35th ESARDA annual meeting, 2013, [Online]. Available: <http://urn.kb.se/resolve?urn=urn:nbn:se:uu:diva-200707>.